Modeling and Optimal Energy-saving Control of Automotive Air-conditioning/Refrigeration Systems

Yanjun Huang[1,*], Amir Khajepour[1], Farshid Bagheri[2], Majid Bahrami[2]

[1]Department of Mechanical and Mechatronics Engineering, University of Waterloo, Ontario, N2L3G1, Canada; [2]School of mechatronic system engineering, Simon Fraser university, Surry, BC, V3T 0A3, Canada

Abstract

Air-conditioning/Refrigeration (A/C-R) systems are extensively adopted in homes, industry, and vehicles. An important step in achieving a better performance and higher energy efficiency for the A/C-R system is a control-based model and a proper control strategy. As a result, a dynamic model based on the moving boundary and lumped parameter method is developed in this paper. Unlike existing models, the proposed model lumps the fins' effects into two equivalent parameters without adding any complexity and considers the effect brought by the superheat section of the condenser, resulting in a model that is not only simpler but also more accurate than the existing models. In addition, a model predictive controller (MPC) is designed based on the proposed model to enhance the energy efficiency of the A/C-R system. Simulation and experimental results are presented to demonstrate the accuracy of the model. The experiments show that about 8% energy saving can be achieved by using the proposed MPC compared to the conventional on/off controller under the examined scenario. The better performance of the proposed controller can appeal the electrification of the automotive A/C-R systems so as to eliminate idling caused by running A/C-R systems when a vehicle stops.

Keywords

Control-based dynamic model; Energy efficiency; Model predictive controller; Automotive A/C-R system Electrification; Idling

*Corresponding author. Tel: +1 226 988 2606
Email addresses: y269huan@uwaterloo.ca (Y.Huang), a.khajepour@uwaterloo.ca (A.Khajepour), fbagheri@sfu.ca (F. Bagheri), mbahrami@sfu.ca (M. Bahrami)

Nomenclature

$h_{ge}\left(h_{gc}\right)$	*enthalpy of vapor refrigerant*	ρ_{ref}	*density of refrigerant*
h_{ic}	*enthalpy of refrigerant at the inlet of condenser*	$\rho_{lc}\left(\rho_{le}\right)$	*density of liquid refrigerant*
h_{ie}	*enthalpy of refrigerant at the inlet of evaporator*	$\rho_{gc}\left(\rho_{ge}\right)$	*density of vapor refrigerant*
h_{is}	*isentropic of refrigerant in compressor*	S	*slip ratio*
$h_{lc}\left(h_{le}\right)$	*enthalpy of liquid refrigerant*	St	*Stanton number*
$h_{lgc}\left(h_{lge}\right)$	*latent enthalpy of refrigerant*	$T_{wfc}\left(T_{wfe}\right)$	*equivalent temperature of tube wall & fin*
h_{oc}	*enthalpy at the outlet of condenser*	$T_{rc}\left(T_{re}\right)$	*saturation temperature of refrigerant*
j	*Calburn factor*	T_a	*air temperature around the heat exchanger*
$L_c\left(L_e\right)$	*total length of the heat exchanger tube*	T_{sh}	*superheat*
$\dot{m}_v$	*refrigerant mass flow rate through the expansion valve*	T_{ic}	*refrigerant temperature at the inlet of condenser*
$\dot{m}_{comp}$	*refrigerant mass flow rate through the compressor*	V_d	*volumetric displacement of compressor*
m_{pipe}	*total refrigerant mass in the pipes*	η_{vol}	*volumetric efficiency of compressor*
m	*total heat exchanger mass*	η_a	*adiabatic efficiency of compressor*
P_c	*pressure of condenser*	$\bar{\gamma}_c\left(\bar{\gamma}_e\right)$	*mean void fraction of two-phase section*
P_e	*pressure of evaporator*	N_{comp}	*compressor speed*
Pr	*Prandtl's number of air*	N_{cond}	*condenser fan control input*
ρ_v	*density of refrigerant through the valve*	N_{evap}	*evaporator fan control input*

1. INTRODUCTION

The continuously increasing demands on lower emission levels and better fuel economy have driven researchers to develop more efficient, less polluting vehicles [1]. However, as the main auxiliary load of vehicles, the A/C-R systems can consume up to 25% of the total fuel or even more in long-haul service vehicles. In addition, as the main energy consumption source in the A/C-R system, the compressor is usually connected directly to the engine via a belt in conventional vehicles, such that engines sometimes have to idle to power the A/C-R system during vehicle stops. For example, long-haul trucks are equipped with a sleeper cabin where the drivers can live on the road [2]. Usually, the trucks idle to provide power to the air conditioning system for cabin temperature control. Similarly, food service trucks need to idle to provide power to the refrigeration system while loading or unloading. When it comes to the vehicle idling, many drawbacks appear, such as the low efficiency of the engine and excessive emissions [3]. Thus, there are significant benefits in operating A/C-R systems efficiently, both in terms of both operating costs and their effects on the environment [4]. An important step in achieving better performance and higher energy efficiency is a control-based model and a proper control strategy [5]. Therefore, making more efficient auxiliary devices can bring many benefits to vehicle owners as well as the environment. But in most conventional vehicles, the compressor speed is proportional to engine speed instead of actively varying with the requirements of passenger or working conditions [6]. This impedes the advanced controller development for the automotive A/C-R system given that the controllers are usually applied to manipulate the speeds of compressor and fans. However, as the development of anti-idling technologies such as the Auxiliary Battery Powered (ABP) units, hybrid electric vehicles (HEVs) and electric vehicles (EV), the on-board energy storage system (ESS) is capable to power the A/C-R system independently such

that the A/C-R system can be disconnected from the engines [7]. That means the electrification of the A/C-R system and then the application of advanced controller in vehicles are possible [6]. As a result, the idling caused by powering auxiliary systems when vehicle stops can be eliminated such that the performance and efficiency of the automotive A/C-R system largely improved [8]. This can be achieved partially by developing advanced controllers to replace the conventional on-off (bang-bang) controllers. The design of advanced controllers requires a control-based model of the A/C-R systems that is accurate but simple enough for real time implementation. A control-based model is actually a trade-off between accuracy and simplicity. If the model is too simple, it will not be able to reflect the main characteristics of the system, which leads to poor closed-loop control performance. On the other hand, if it is too complex, it slows down the controller by increasing computation time, which may not be used in real-time implementations [9], though it can describe the dynamics of the system well enough and produce good predictions. Consequently, this paper presents a simplified but accurate model for the A/C-R systems that has been validated by experimental results, and then the controllers are designed based on the proposed model.

This paper is organized as follows: a literature review on the existing dynamic models of A/C-R system is presented in the second section; next, a moving boundary and lumped parameter model is developed. The parameters of the model are identified in the following section. Then, a brief introduction of the experimental system as well as the simulation and experimental results are given for comparison and model validation. Furthermore, an on/off controller and a discrete MPC are developed, simulated, validated experimentally and compared in next section. In the last section, comments and future work are discussed.

2. Previous Research

Overall, there are four main components in a vapor compression cycle: the compressor, evaporator, expansion valve and condenser. The dynamics of other auxiliary components such as the accumulator and receiver are incorporated into the connecting pipes or two heat exchangers. In the literature, the modeling of compressor and expansion valve, regardless of their types (electric, thermostatic or automatic expansion valve), is demonstrated by algebraic empirical equations [10]. This is because the dynamics of a compressor and expansion valve is an order of magnitude faster than those of heat exchangers (evaporator and condenser) [11].

Several types of models have been built for heat exchangers for different purposes. For example, discretized or finite difference models are more accurate and are usually used in many commercial software packages. These types of models can result in increased accuracy in prediction [12]; however, it is too complicated to be used in real-time control strategy development and implementation. Another type of heat exchanger model is based on lumped parameters and is usually a first order time invariant dynamic model; however, it has oversimplified most of the dynamic characteristics of heat exchangers [13]. Above all, the most popular modeling approach is the moving-boundary/interface lumped-parameter method, which is capable of capturing the dynamics of multiple fluid phase heat exchangers while keeping the simplicity of lumped parameter models [13]. Wedekind *et al*. [14] contributed significantly by simplifying a class of two-phase transient flow problems into the type of lumped-parameter

systems. With experimental confirmation, the authors showed that the mean void fraction, i.e., the volumetric ration of vapor to total fluid of the two-phase region in a heat exchanger remains relatively unchanged. This suggests that it will stay invariant, regardless of how the refrigerant distributes throughout the heat exchanger and how the length of two-phase region changes [11]. With this assumption, this method allows the two-phase section to be modeled with lumped parameters. In this way, the whole model can be much more simplified than the discretized model. On the other hand, based on the first law of thermodynamics, the dynamics of the length of the two-phase section (the movement of the interface between different regions) can be determined.

X. D. He [11] used the moving interface lumped parameter modeling method. Based on several assumptions such as assuming the heat exchanger is a long, thin, and horizontal tube, He developed the complete evaporator and condenser nonlinear dynamic model with more than five states for each of them, and then derived the entire system model by considering the boundary conditions of all the components. However, in his research, only the linearized model was partially verified.

In recent years, A. G. Alleyne and his teammates have improved the model derived by X. D. He. For instance, Bin Li in [15] built a model for startup and shutdown periods by considering different distributions of the refrigerant inside the heat exchangers. B. P. Rasmussen and A. G. Alleyne in [13] modeled the auxiliary components such as the accumulator and receiver. Parameter identification algorithms for A/C-R system modeling have also been improved in [16] by B. D. Eldredge. Furthermore, some special architectures of vapor compression cycle system that were modeled in [17] by Joseph M. Fasl. [18-20] further validated their models experimentally, and it showed overall improvements over the previous models. More importantly, Thomas L. McKinley *et al.* [21] considered the fins' effects by introducing several other parameters such as "fraction of refrigerant-to-structure surface area on fins and refrigerant-side fin efficiency", which makes the model more complex with 9 states in evaporator alone. In all the models above, there are more than ten states representing the complexity of the model which makes it difficult to guarantee the real-time running of controllers developed based on these models. That is why X. D. He [22] developed a simple model of the whole system by assuming the identical temperature of heat exchanger wall and reduced the number of states to five. In addition, a Gain Scheduling LQG was developed by using this simplified model. Unfortunately, the simplified model has not been validated experimentally.

The drawbacks of the models existing in literatures are elaborated as follows. Firstly, the complete models with more than ten states are too complex to be used to develop controllers. Secondly, the simple model does include fins' effects when modeling heat exchangers, which brings discrepancies to the model. As a result, this paper is intended to further improve the accuracy of model in [21] by incorporating the fins in the model of heat exchangers in a new way without adding the complexity of the model. The proposed model is validated experimentally and compared with the existing one.

In this paper, an advance MPC is designed for the A/C-R system for HEVs, EVs and conventional vehicles with ABPs, where the

A/C-R systems can be directly powered by the on-board ESS. First of all, a simplified control-oriented dynamic model of the automotive A/C-R system is developed, where only six states instead of more than ten reported in the literature are used. In order to keep the accuracy of this simplified model comparable to high order models, the fins' effects are considered and lumped into two equivalent parameters. In addition, the effects of the superheat section of in the condenser are also included into the model by studying the experimental data instead of the model used in [22]. This model is simulated and experimentally validated under several scenarios. The results show that this model is simple and accurate enough to be used in real-time control systems. Using this model, an energy-saving MPC is designed and its performance is compared with the conventional on/off controller. Due to some discrete constraints, this MPC is designed as a discrete MPC, which is seldom mentioned in the existing literature. In addition, since the A/C-R system operation increases the fuel consumption by 90% at the maximum during the vehicle idling [23], this work is an important step in developing anti-idling technologies for conventional vehicles. For example, better performance and higher energy efficiency brought by the proposed MPC can appeal the electrification of automotive A/C-R system so as to reduce vehicle idling. Furthermore, this fast and robust MPC can always guarantee the minimum power consumption for A/C-R systems under any working conditions. Due to the relatively slow dynamics of the working conditions of A/C-R systems, this slowly changing power consumption information can be integrated into the power management strategy as the auxiliary power taken out of the energy storage system [24] for the state of charge (SOC) prediction to enhance the overall efficiency of the HEVs and EVs.

3. Model

An A/C-R system or a vapor compression cycle generally consists of four main components as shown in Fig. 1, where the evaporator and condenser are divided into several sections under normal working conditions. There are two sections, i.e., two-phase and superheated sections in the evaporator and three sections, i.e., superheated, two-phase, and subcooling sections in the condenser. The valve is used to uphold the pressures of the two heat exchangers, while the compressor sends the refrigerant from low-pressure heat exchanger to high-pressure heat exchanger.

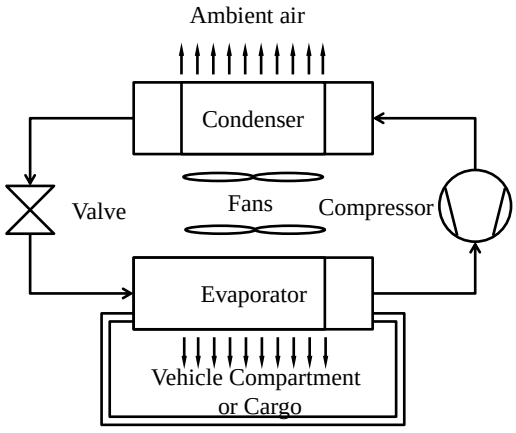

Fig. 1. Schematic diagram of A/C-R system

The working principle of the A/C-R system is briefly described below. The refrigerant before entering the evaporator is

characterized by low pressure, low temperature and two-phase state. In the evaporator, it will absorb heat from the specific space and change into vapor phase after exiting from the evaporator. The vapor refrigerant is compressed by the compressor and turned into high pressure and high temperature vapor. It will then be sent to the condenser where the removal of its heat results in a high-pressure and low-temperature liquid phase. Finally, after going through the expansion valve, the pressure will drop to the evaporator pressure and the liquid refrigerant will be changed into the two-phase state. The same cycle will repeat again.

As is well known, the dynamics of the valve and compressor is so fast with respect to the cooling process that they can be treated by some empirical equations obtained from test data. However, for the two heat exchangers, evaporator and condenser, due to their complex nature, the moving boundary and lumped parameter modeling methods will be employed to develop their control- based dynamic model.

In the vapor compression system modeled and experimentally validated in this work, the expansion valve is a thermostatic expansion valve, which adjusts its opening degree according to the refrigerant temperature (superheat temperature) at the outlet of the evaporator. The evaporator is a fin-tube type and the condenser is a micro-channel type as shown in Fig. 2 and Fig. 3. The refrigerant used is R134a [25]. This section only elaborates the main dynamic equations. For the complete version nonlinear and linearized model for MPC development, please refer to Appendix I.

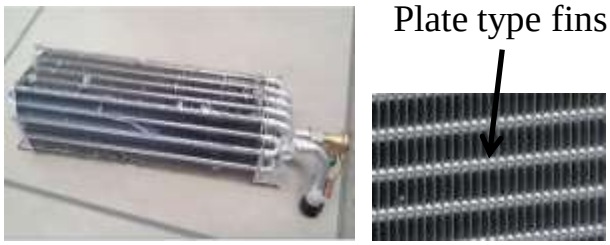

Fig. 2. Fin-tube type evaporator with plate fins

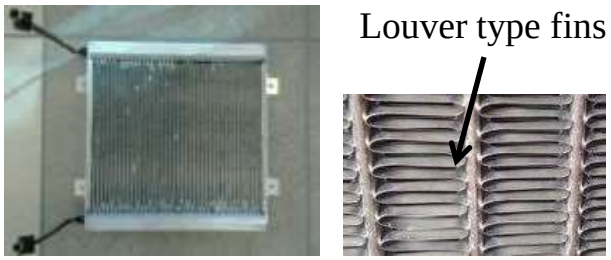

Fig. 3. Micro-channel type condenser with louver fins

3.1. Thermostatic Expansion Valve

The expansion valve is assumed to be isenthalpic *i.e.* the enthalpy at the inlet of the valve is identical to that at the outlet [16]. The other important parameter is the refrigerant mass flow rate $\dot{m}_v$ through the expansion valve that is modeled by

$$\dot{m}_v = C_v A_v \sqrt{\rho_v (P_c - P_e)} \tag{1}$$

where, P_c and P_e are the pressures of condenser and evaporator; ρ_v is the refrigerant density at the inlet of the valve; C_v represents the discharge coefficient mapped as a polynomial correlation $\left(C_v = f_C(P_c - P_e)\right)$ of the pressure difference between evaporator and condenser; A_v refers to the area of the valve opening mapped as a polynomial correlation $\left(A_v = f_A(P_{sat} - P_e)\right)$ of the pressure difference between evaporator and the saturation pressure of the evaporator outlet temperature. These correlations can be obtained by experimental data. The remaining parameters such as density can be obtained by the thermodynamic properties [25] of the

refrigerant built in lookup tables.

3.2. Compressor Model

The dynamics of the compressor can be demonstrated by

$$\dot{m}_{comp} = N_{comp} V_d \eta_{vol} \rho_{ref} \left(P_e\right) \tag{2}$$

$$h_{oc} = \eta_a \left(h_{is}\left(P_e, P_c\right) - h_{ic}\left(P_e\right)\right) + h_{ic}\left(P_e\right) \tag{3}$$

where, $\dot{m}_{comp}$ represents the refrigerant mass flow rate throughout the compressor; N_{comp} means the compressor speed; V_d refers to the volumetric displacement of compressor; ρ_{ref} is the density of refrigerant inside compressor; h_{oc} represents the enthalpy at the outlet of compressor; h_{ic} is the enthalpy at the inlet of compressor; $h_{is}\left(P_e, P_c\right)$ refers to the isentropic enthalpy during the compression process, which can be found by thermodynamic property of the refrigerant; η_{vol} and η_a are volumetric efficiency and adiabatic efficiency, which can be obtained by polynomial correlations $\left(\eta_{vol} = f_{vol}(N_{comp}, P_c - P_e), \eta_a = f_a(N_{comp}, P_c - P_e)\right)$ with respect to the speed of compressor and two pressures [13, 16, 26].

3.3. Fin-tube Type Evaporator

Basically, two common types of heat exchangers are used in A/C-R systems: Fin-tube type and Micro-channel type. In the experimental system of this study, the fin-tube type evaporator as seen in Fig. 2 is used.

Under normal working conditions, the evaporator can be divided into two sections: the two-phase section and the superheated section. The modeling is based on the whole heat transfer process: the heat convection between refrigerant inside the evaporator tube and tube wall & fins, the heat conduction throughout the tube wall & fins, and the heat convection between the tube wall & fins and the ambient fluid like air. This process is applied to the two sections. Based on the energy conservation of the heat transfer process and the mean void fraction concept mentioned in the previous section, the dynamic equations for each section can be obtained. Furthermore, the whole heat exchanger model can be developed by considering the boundary conditions between different sections [9, 10].

All the heat exchanger models in the literature are based on a long, thin, one-dimensional tube assumption. They do not consider the fins' effects or consider them in a complicated way [18] when modeling the heat convection between the tube wall and the refrigerant inside. However, from Fig. 2 and Fig. 3, it can be seen that there are many fins (plate type or louver shape type) around the tube walls. Usually the fins and tubes are made from the same material. If it is not considered, the heat conduction throughout the fins would introduce inaccuracy to the model.

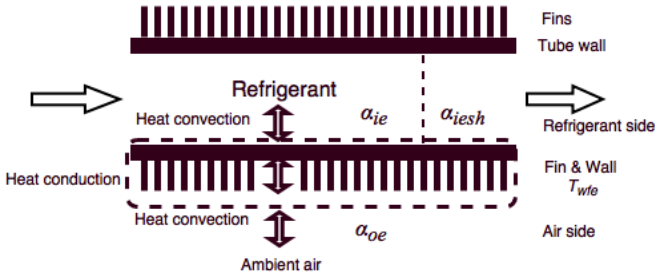

Fig. 4. Schematic of evaporator with equivalent parameters

Unlike the thin tube wall where no temperature gradient is assumed, the fins are long, and a one-dimensional temperature gradient exists along the length of the fins. This gradient is dependent on the structure of the fins and difficult to simulate. However, from the perspective of energy conservation, the energy transferred from the refrigerant to the tube wall and fins is identical to the energy taken away by the air and the energy kept in the wall and fins due to their thermal inertia. In this way, the wall and fins could be lumped together shown in dotted box of Fig. 4. Thus, it is reasonable to utilize an equivalent temperature T_{wfe} to represent the temperature of wall and fins. The other equivalent parameter used is the refrigerant-side heat transfer coefficient. In evaporator, α_{ie} and α_{iesh} are provided to represent the coefficients for the two-phase section and the superheat section respectively. After applying these equivalent parameters, the simplified nonlinear dynamic model of the evaporator can be written as [11, 22]:

$$h_{lge}\rho_{le}\left(1-\bar{\gamma}_e\right)A_e\frac{dl_e}{dt}=\dot{m}_v\left(h_{ge}-h_{ie}\right)-\alpha_{ie}\pi D_{ie}l_e\left(T_{wfe}-T_{re}\right) \tag{4}$$

$$A_eL_e\frac{d\rho_{ge}}{dP_e}\frac{dP_e}{dt}=\dot{m}_v\frac{h_{ie}-h_{le}}{h_{lge}}-\dot{m}_{comp}+\frac{\alpha_{ie}\pi D_{ie}l_e\left(T_{wfe}-T_{re}\right)}{h_{lge}} \tag{5}$$

$$\left(C_pm\right)_{wfe}\frac{dT_{wfe}}{dt}=\alpha_{oe}A_{oe}\left(T_{ae}-T_{wfe}\right)-\alpha_{ie}\pi D_{ie}l_e\left(T_{wfe}-T_{re}\right)-\alpha_{iesh}\pi D_{ie}(L_e-l_e)\left(T_{wfe}-T_{re}\right) \tag{6}$$

where, the three states refer to the length $\left(l_e\right)$ of the two-phase section, the pressure $\left(P_e\right)$ of the evaporator, and the equivalent temperature $\left(T_{wfe}\right)$ of tube wall & fins. Equation (4) simulates the energy transfer from the refrigerant to the heat exchanger tube wall & fins of the two-phase section. The first term on the right-hand side of this equation shows the energy change after the refrigerant goes through the two-phase section; h_{ge} is the enthalpy of the vapor refrigerant under the current pressure, or the enthalpy at the boundary of the two sections, and h_{ie} is the enthalpy of the refrigerant at the inlet of the evaporator. The second term describes the energy absorbed from the evaporator tube wall and fins of two-phase section where D_{ie} is the inner diameter of the tube, and T_{re} is the saturation temperature of the refrigerant under the current pressure. Thus, the difference of these two terms represents the energy absorbed/rejected by the two-phase section or the energy needed to evaporate the liquid refrigerant in the two-phase section. Based on this energy change, the two-phase length change can be obtained by using the left-hand side term

where h_{lge} means the latent enthalpy; ρ_{le} is the liquid refrigerant density; $(1-\bar{\gamma}_e)$ is the liquid volumetric fraction of the two-phase section, and A_e is the sectional area of the tube [18]. All the enthalpies $(h_{ge}, h_{ie}, h_{lge})$, densities/density variation with respect to pressure $\left(\rho_{le}, \rho_{ge}, \rho_{ie}, \frac{d\rho_{ge}}{dP_e}\right)$ and temperature (T_{re}) of the refrigerant can be obtained by lookup tables built according to thermodynamic properties [25] of the used refrigerant; whereas, the heat transfer coefficients are identified by experimental data and shown in Table 1.

Equation (5) denotes the vapor refrigerant change rate throughout the evaporator tube. The first term on the right-hand side of this equation refers to the vapor mass at the inlet of the evaporator. As is known, the refrigerant will become a two-phase refrigerant after going through the expansion valve liquid. Based on the enthalpy (h_{ie}) of refrigerant, liquid enthalpy (h_{le}) and latent enthalpy (h_{lge}) the liquid percentage at the inlet of the evaporator can be found. The second term represents the mass flow rate leaving evaporator; whereas, the third term is the vapor refrigerant changed from liquid. The left hand side is the vapor mass change rate inside the evaporator. The pressure change rate can be found via the density change rate by using the chain rule where L_e means the total length of the evaporator tube wall, and ρ_{ge} is density of the vapor refrigerant under the current evaporator pressure (P_e).

Equation (6) reflects the heat conduction of the whole heat transfer process. The first term on the right-hand side refers to the total energy transferred to the tube wall & fins from the ambient air, and α_{oe} is the heat transfer coefficient, which can be found by Colburn J-factor correlation; A_{oe} represents the total outside area of the tube wall as well as fins; T_{ae} is the mean air temperature. The last two terms refer to the energy transferred from the tube wall & fins to the refrigerant in the two-phase section and the superheated section, respectively; whereas, α_{iesh} refers to the heat transfer coefficient in superheat section. The left-hand side shows the change of the temperature of the tube wall & fins because the mass m and C_p are the total mass and specific heat of the tube wall & fins.

Since the equivalent wall and fins temperature is defined based on energy conservation, it is not the temperature of the wall or fins, so it could not be measured directly. After lumping the fins and the wall together, the Pierre's correlation [11] for calculating refrigerant-side heat transfer coefficient is no longer suitable. However these equivalent parameters could be identified easily by Equation (5, 6).

3.4. Micro-channel Type Condenser

As is mentioned above, the micro-channel type condenser is modeled and used in the experimental work. It can be seen from Fig. 3 that many louver-shape fins are around each tube. There are many parallel micro-channels inside each tube. Under normal working conditions, the refrigerant distribution is more complex than that of the evaporator.

The condenser can be divided into three sections; however, in order to simplify the model for the purpose of real-time application, the study of the experimental data suggests that the subcooling section could be neglected due to the much lower subcooling temperature (about $2\,^{\circ}C$) as compared to the superheat temperature (about $50\,^{\circ}C$). Another reason is that the energy rejected to generate this lower subcooling temperature is also relatively small. Besides that, the small energy error caused can be compensated by the equivalent heat transfer coefficient of two-phase section. To make up for this subcooling section from a temperature aspect, the refrigerant temperature at the outlet of the condenser could be found by experimental data. Using the above assumptions, the condenser equations can be obtained in a similar manner to those of the evaporator.

It is known that the total mass m_{total} of the refrigerant inside the cycle is constant without considering the leakage. The mass of refrigerant outside of the two heat exchangers is defined as m_{pipe}. Therefore, the difference between these two masses represents the mass inside the evaporator and the condenser, which can be shown by [13],

$$m_{total} - m_{pipe} = A_e\left[\rho_{le} l_e \left(1-\bar{\gamma}_e\right) + \rho_{ge} l_e \bar{\gamma}_e + \rho_{she}\left(L_e - l_e\right)\right] + A_c\left[\rho_{lc} l_c \left(1-\bar{\gamma}_c\right) + \rho_{gc} l_c \bar{\gamma}_c + \rho_{shc}\left(L_c - l_c\right)\right] \tag{7}$$

The first term of the right-hand side refers to the refrigerant mass of both vapor and liquid inside the evaporator, the second term to that inside the condenser; whereas, l_c and $\bar{\gamma}_c$ are the length and mean void fraction of the two-phase section of the condenser. Therefore, from Equations (4) and (7), the two-phase length of condenser can be found. As a result, there are only two states, pressure $\left(P_c\right)$ and equivalent temperature $\left(T_{wfc}\right)$ with which the condenser equations similar to the evaporator can be written as [22]:

$$A_c L_c \frac{d\rho_{gc}}{dP_c}\frac{dP_c}{dt} = \dot{m}_{comp} - \frac{\alpha_{ic}\pi D_{ic} l_c \left(T_{rc} - T_{wfc}\right)}{h_{lgc}} \tag{8}$$

$$\left(C_p m\right)_{wfc}\frac{dT_{wfc}}{dt} = \alpha_{oc}\left(N_{cond}\right)A_{oc}\left(T_{ac} - T_{wfc}\right) - \alpha_{ic}\pi D_{ic} l_c \left(T_{wfc} - T_{rc}\right) - \alpha_{icsh}\pi D_{ic}\left(L_c - l_c\right)\left(T_{wfc} - \left(T_{rc} + T_{ic}\right)/2\right) \tag{9}$$

The meanings and acquisition methods of all the parameters used in the above equations can be referred to the explanations of Equation 5 and Equation 6.

3.5. Pipes

In the vapor compression cycle, the four main components are connected by several pipes of different sizes. Usually, the pipes are assumed to be adiabatic, and the pressure loss is neglected because of the short length. The refrigerant mass inside the pipe is m_{pipe}, and it is estimated by the length and inner diameter of each piece of pipe. Using the pressure inside the pipe, the density is found. The state of refrigerant in each pipe is assumed to be uniform except for the one between the expansion valve and evaporator, where the refrigerant is in two-phase state. The vapor percentage can be approximated by $\left(h_{ie} - h_{le}\right)/h_{lge}$ as explained in the evaporator model.

4. Parameter Estimation

In the vapor compression cycle model, there are three kinds of parameters: physical parameters, empirical parameters and identified parameters.

4.1. Physical Parameters

The physical parameters such as the dimensions of pipes, lengths, inner and outer diameters, interior and exterior areas of heat exchangers can be easily measured or obtained from the manufacturers.

4.2. Empirical Parameters

Empirical parameters can be estimated by empirical equations obtained from experimental data. Most of these parameters vary with working conditions. Therefore, each parameter should be calculated on-line to update its value. For each parameter, several correlations may exist. In the following section, the mean void fraction and the air-side heat transfer coefficient will be discussed in more detail.

4.2.1. The mean void fraction $\bar{\gamma}$

The mean void fraction $\left(\bar{\gamma}\right)$ is defined as the ratio of vapor volume to total volume in two-phase region, and has been employed to describe the characteristics of two-phase flows [16]. Wedekind *et al*. mentioned that the mean void fraction can be assumed invariant during transient processes [14]. However, recently this parameter is assumed to be changed with the fluid quality, and it is defined as the ratio of vapor mass to total mass entering the heat exchangers and calculated by [15, 19]

$$\bar{\gamma} = \frac{1}{\beta} + \frac{1}{x_2 - x_1}\left[\frac{\alpha}{\beta}\ln\left(\frac{\beta x_1 + \alpha}{\beta x_2 + \alpha}\right)\right] \tag{10}$$

with, $\alpha = \left(\frac{\rho_g}{\rho_f}\right) S$ and $\beta = 1 - \alpha$

where, S is the slip ratio defined as the ratio of vapor velocity and liquid velocity in two-phase sections and identified by test data. x_1 and x_2 are the fluid quality at the inlet and outlet of two-phase section, respectively.

4.2.2. Air-side heat transfer coefficient α_o

The air-side heat transfer coefficient is related to the energy transferred from the heat exchanger tube wall & fins. But, for different kinds of fins, there are different empirical correlations. In this study, the Colburn j factor is used, which gives a way of relating Reynolds number of airflow through a heat exchanger with experimentally determined heat transfer characteristics of the heat exchanger [13, 17]. The air-side heat transfer coefficient can be found from *j* factor by using,

$$j = StPr^{2/3} \tag{11}$$

where, Colburn *j* factor is related to Reynolds number and the physical structure of the heat exchanger. For the fin-tube type evaporator, please refer to [27], and for the micro-channel condenser, refer to [28]. Prandtl's number *Pr* is calculated at air temperature; Stanton number St [13] is related to air-side heat transfer coefficient and defined by

$$St = \alpha_o / \left(GC_p \right) \tag{12}$$

where, G refers to the air mass flux across the heat exchanger and C_p is the thermal conductivity of air at air temperature. By reconstructing the above two equations, the heat transfer coefficient becomes

$$\alpha_o = jGC_p / Pr^{2/3} \tag{13}$$

4.2.3. Mean air temperature around heat exchangers T_a

This parameter can be assumed as the mean temperature of the air temperature at the inlet and outlet of the heat exchanger [13]. Taking the evaporator as an example, in order to find the air temperature at the outlet of the heat exchanger, T_{ae} should be calculated beforehand by

$$T_{ae} = \left(2\left(\frac{\dot{m}_{air\_e} C_{p,air}}{\alpha_{oe} A_{oe}} \right) T_{a,in} + T_{wfe} \right) \Bigg/ \left(2\left(\frac{\dot{m}_{air\_e} C_{p,air}}{\alpha_{oe} A_{oe}} \right) + 1 \right) \tag{14}$$

where, $\dot{m}_{air\_e}$ refers to the air mass flow rate going through the evaporator while $C_{p,air}$ means the specific heat of the air. In this process, $\dot{m}_{air\_e}$ is proportional to the evaporator fan control signal N_{evap}. This proportional coefficient can be identified by using experimental data. T_{ac} at the condenser side can be calculated in a similar manner. $T_{a,in}$ is the air temperature at the inlet of evaporator and measured by thermal couples.

4.3. Identified Parameters

Identified parameters, such as the equivalent refrigerant-side heat transfer coefficients and the equivalent temperature of wall & fins, refer to those that are obtained by experimental data. Regarding the steady state test for parameter identification, the system is fed by three inputs and the two temperatures shown in the known parameters column of Table 1. After running for about 30 minutes, the system approaches the steady state. The data of temperatures, pressures, and refrigerant mass flow are collected by using the sensors mentioned in experiments and model validation section. The parameters and states in the identified parameter column are identified off-line by using the least square method based on the collected data.

Table 1 the known and identified parameters at one steady state

Known parameters	***Values***	***Identified parameters***	***Values***
$N_{comp}(rpm)$	4500	$l_e(m)$	2.0137
$N_{evap}(Hz)$	41.3	$l_c(m)$	0.2528
$N_{cond}(Hz)$	52.5	$T_{wfe}(^{\circ}C)$	3.84
$T_{e\_air\_in}(^{\circ}C)$	20	$T_{wfc}(^{\circ}C)$	33.9
$T_{c\_air\_in}(^{\circ}C)$	27	$\alpha_{ie}(kw/(m^2K))$	0.68
$P_e(bar)$	2.23	$\alpha_{ic}(kw/(m^2K))$	1.9
$P_c(bar)$	8.95	$\alpha_{iesh}(kw/(m^2K))$	0.045
$T_{sh}(^{\circ}C)$	2.74	$\alpha_{icsh}(kw/(m^2K))$	0.13

The known parameters include the inputs of the system, the working conditions as well as the measurements; whereas, the identified parameters consist of immeasurable states and refrigerant-side heat transfer coefficients. Here, the equivalent two-phase heat transfer coefficient, α_{ie}, for evaporator is elaborated. From Table 1, this parameter for evaporator is 0.68 $kw/\left(m^2K\right)$; whereas, the reported value in the literature is usually between 1 and 5 $kw/\left(m^2K\right)$. That is because after considering the fins' effects, the identified equivalent temperature of the tube wall & fins T_{wfe}, becomes higher than the temperature of the exact tube wall at the evaporator side. The temperature difference $\left(T_{wfc}-T_{rc}\right)$ from the refrigerant saturation temperature at the current pressure is larger too. In order to balance the transferred energy of the two-phase section $\alpha_{ie}\pi D_i l_e\left(T_{wfc}-T_{rc}\right)$, the equivalent heat transfer coefficient must be smaller than that estimated by Pierre's empirical correlation [19]. As a result, this coefficient is called the equivalent coefficient, and the same thing happens for its counterpart of the condenser.

5. Implementation and simulation

By considering the components' boundary conditions (*e.g.* the temperature and enthalpy at the outlet of evaporator are identical to those at the inlet of the compressor), the whole cycle can be simulated using the above model (Equations (1) to (14)). In this model, the inputs are compressor speed N_{comp}, the control frequencies of evaporator and condenser fan $\left(N_{evap},N_{cond}\right)$, which are proportional to the two fan speeds. The air temperatures at the inlet of the evaporator and condenser are assumed to be measured and known as $\left[T_{e\_air\_in},T_{c\_air\_in}\right]$. The five model states $\left[P_e,P_c,l_e,T_{wfe},T_{wfc}\right]$ refer to the pressures of the evaporator and the condenser, the two-phase section lengths and equivalent tube wall & fins temperatures of two heat exchangers. Many outputs can be calculated by this model, including air temperature at the outlet of evaporator, which is related to the cooling capacity of the system. The initial conditions and parameters were estimated off-line by using steady state test data. The model was built into MATLAB/Simulink.

6. Experiments and Model Validation

In this section, the experimental system is briefly introduced, and then the model validation work is done under different scenarios.

6.1. Experimental System

In order to verify the developed model, an experimental system provided by one of the industrial partners used for a truck is built to simulate the real operating conditions of an A/C-R system. The schematic of the whole experimental system is shown in Fig. 5, where the condenser-side environmental chamber can provide air at any desired temperature and humidity for the condenser to simulate the ambient temperature. The evaporator and condenser units are connected by pipes via thermostatic valve and compressor to two environmental chambers.

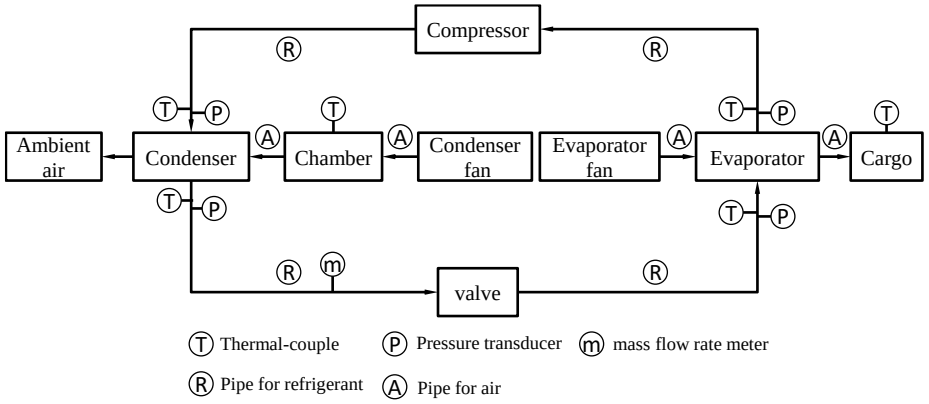

Fig. 5. Schematic of the whole experimental system

In order to identify and validate the proposed simplified model, many sensors are installed at different locations for measurement. The Micro Motion 2400S transmitter with 0.5% accuracy from Emerson Electric Co. is utilized to log the refrigerant mass flow rate, and it is located between the condenser and the thermostatic expansion valve. T-type thermocouples and pressure transducers model PX309 manufactured by OMEGA with 0.25% accuracy are installed on four locations of the whole system to measure both the high and low temperatures/pressures of the refrigerant. Other T-type thermocouples and wind sensor model MD0550 from Modern Device are installed at 8 locations on the evaporator and condenser air streams. Also, The DAQ system (NI CompactDAQ 8-Slot USB Chassis) of NI is employed to collect data from the thermo-couples, pressure transducers, DC power supply and flow meters, and send them to a computer. LabVIEW software is employed to obtain all the measured data from the equipment and save them in an EXCEL file.

The two fans of the evaporator and condenser are controlled by two variable frequency drives (VFD) of YASKAWA (GPD 315/V7) such that the speed could be represented by frequency. While the compressor only has three different speeds, a NI relay module (NI 9485) is used to switch between the three discrete speeds.

6.2. Model Validation

Using the experimental setup, different experiments are conducted, where some are used for parameter identifications and the rest for model validation. For the simulation work, the initial conditions and unknown parameters are identified off-line by one set of experimental data as stated in parameter identification section, and the model is evaluated using the other unseen data. In the following, several other sets of data are used to validate the model by comparing the experimental and simulation results in three different scenarios.

In the first scenario, the speeds of the condenser fan and the compressor change while the speed of the evaporator fan remains unchanged during the 5500-seconds simulation as seen in Fig. 6. Fig. 7 shows the air temperature at the outlet of condenser and evaporator while the inlet temperatures are measured and fed to the model. The air temperature at the outlet agrees with test data but with a little discrepancy, which is probably caused by using the constant refrigerant-side heat transfer coefficient. For the sake

of more accurate more, in the future, this coefficient should be identified on-line. In order to keep the superheat at a certain degree, the expansion valve has to turn down or turn up. As a result, the real temperature at the outlet of evaporator always oscillates. Given that the thermostatic valve model is identified by steady state data, it is difficult to simulate this oscillation, but this phenomenon could be overcome by the use of dynamic test data in the future. Thus, the simulation result is located in almost the middle of the test data; whereas, the temperature at the inlet has a great match between simulation results and test data shown in Fig. 8. In Fig. 9, the simulation results of the refrigerant temperature at the condenser side also fit the test data. Fig. 10 describes good agreements between actual evaporator and condenser pressures and model prediction.

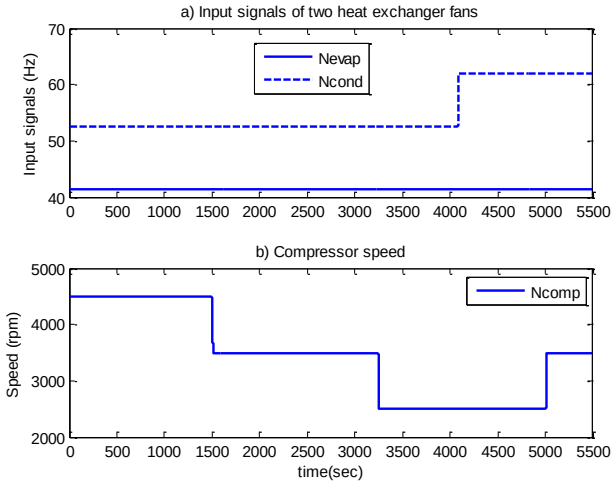

Fig. 6. Inputs of the system

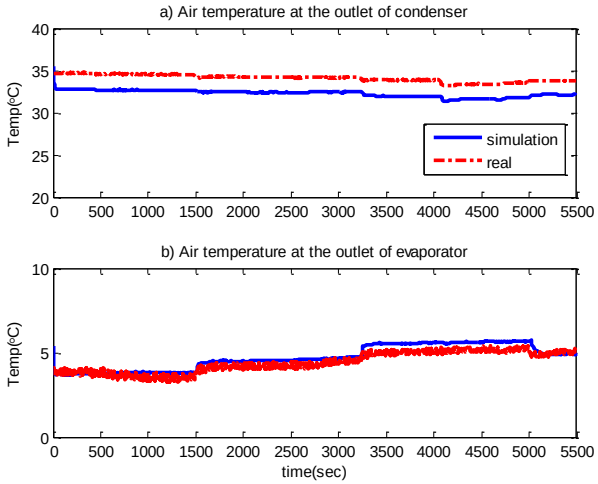

Fig. 7. Air temperature at the outlet of two heat exchangers

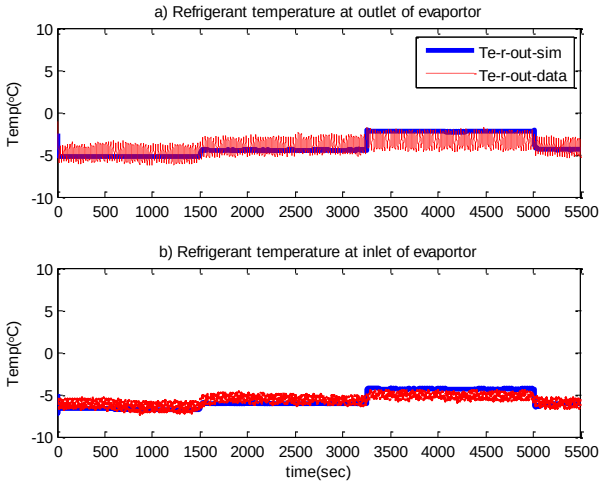

Fig. 8. Refrigerant temperature at inlet and outlet of evaporator

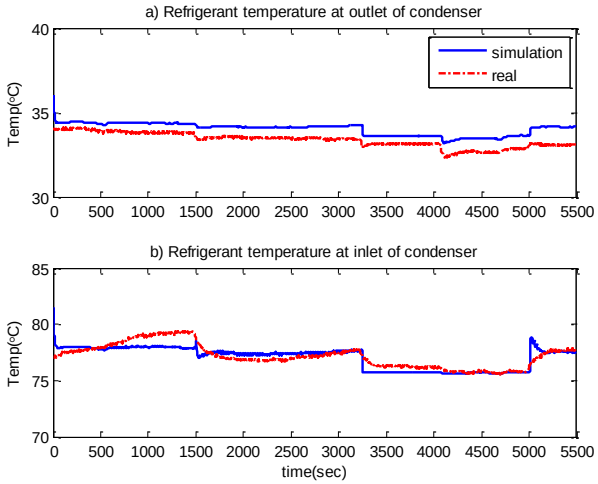

Fig. 9. Refrigerant temperature at inlet and outlet of condenser

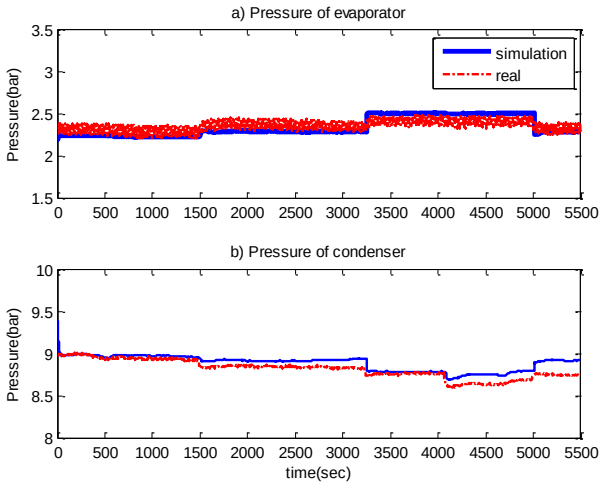

Fig. 10. Pressures of evaporator and condenser

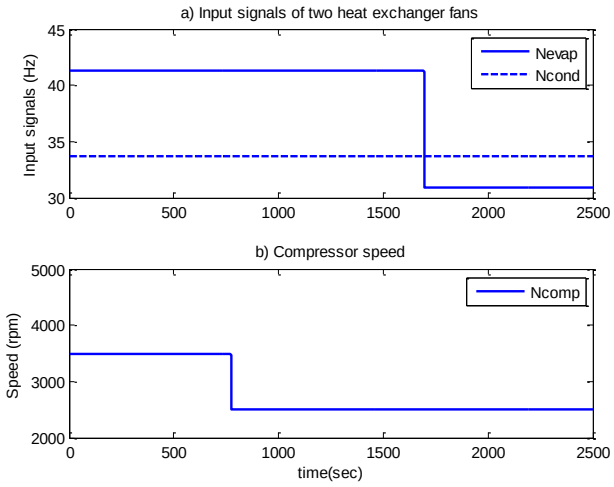

Fig. 11. Inputs of the system

In the second scenario, the speeds of the evaporator fan and the compressor are varied and the speed of condenser fan is invariant.

From Fig. 11 to Fig. 15, conclusions similar to those from the first scenario can be drawn during the 2500-second simulation.

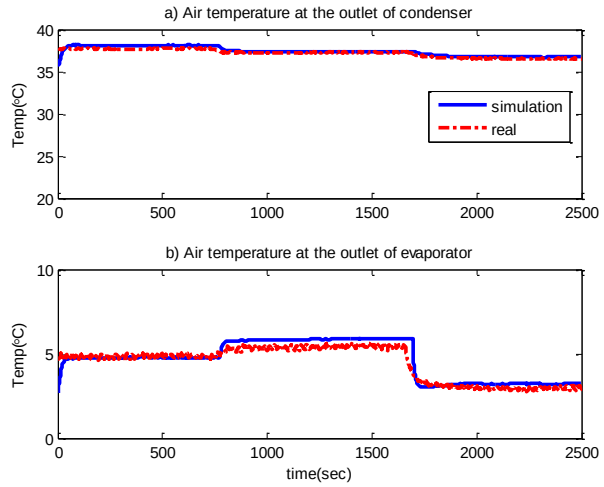

Fig. 12. Air temperature at the outlet of two heat exchangers

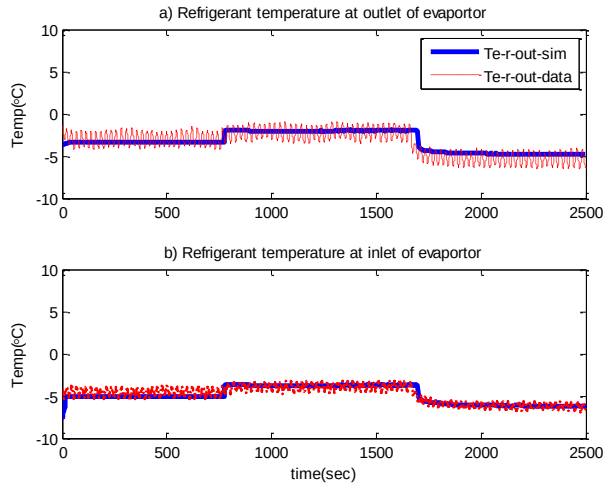

Fig. 13. Refrigerant temperature at inlet and outlet of evaporator

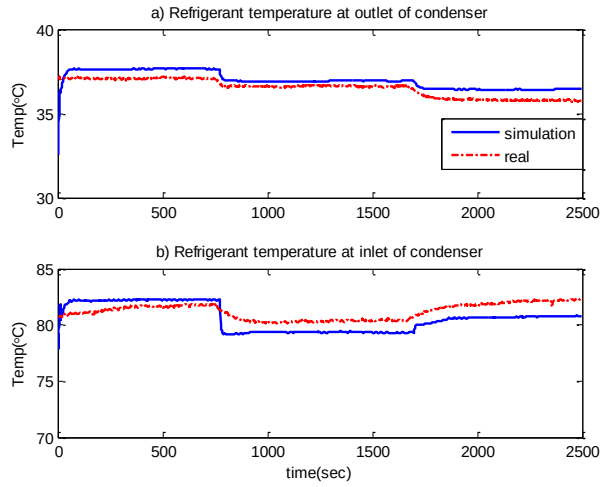

Fig. 14. Refrigerant temperature at inlet and outlet of condenser

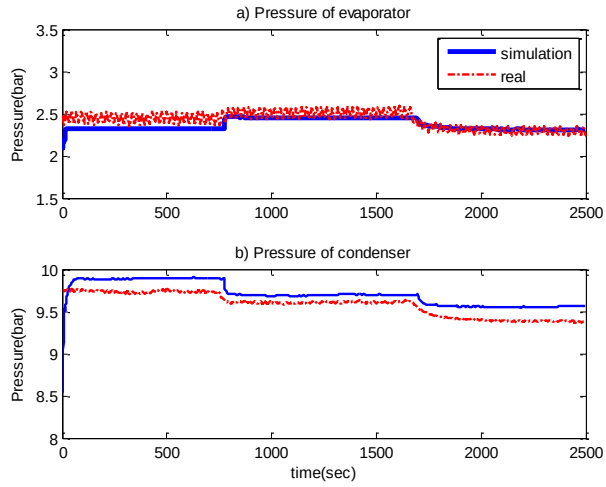

Fig. 15. Pressures of evaporator and condenser

In the last scenario, the input pattern is more complex; at the 560th second, three inputs were changed as depicted in Fig. 16.

However, from Fig. 17 to Fig. 20, it can be seen that the simulation results also fit the test data. However, due to the high nonlinear nature of the system, any system parameter can be affected by each of the three inputs. Taking the evaporator pressure in Fig. 20 for example, it can be seen that it is influenced by both N_{evap} and N_{comp}. The pressure increases as N_{comp} decreases, and decreases N_{evap} as decreases. That is why at the 560th second, the evaporator pressure does not change very much. While in Fig. 18, the refrigerant temperatures are closely related to the evaporator pressure. The temperature at the inlet of evaporator is the saturation temperature under the evaporator pressure, and the temperature at the outlet of the temperature is the sum of the saturation temperature and the superheat temperature. That is why they remain fairly constant when inputs are changed.

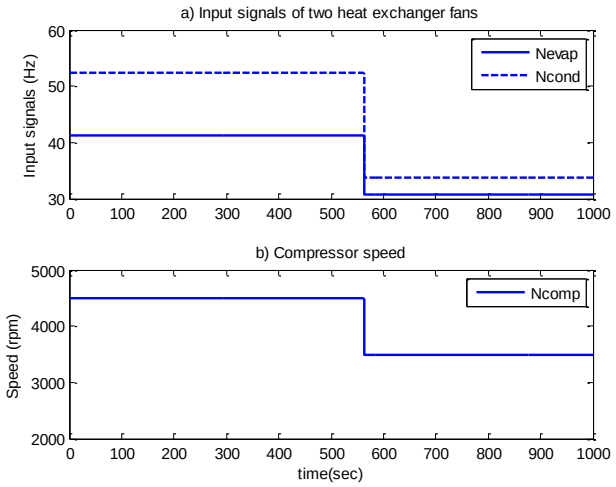

Fig. 16. Inputs of the system

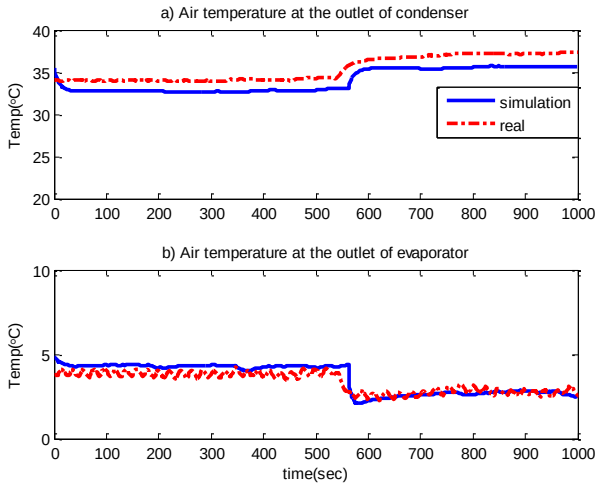

Fig. 17. Air temperature at the outlet of two heat exchangers

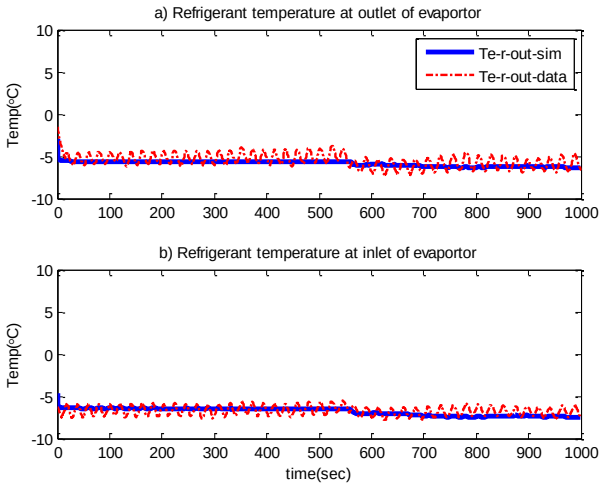

Fig. 18. Refrigerant temperature at inlet and outlet of evaporator

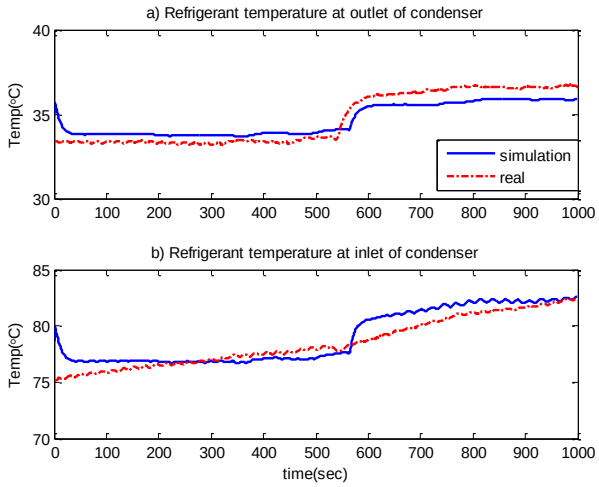

Fig. 19. Refrigerant temperature at inlet and outlet of condenser

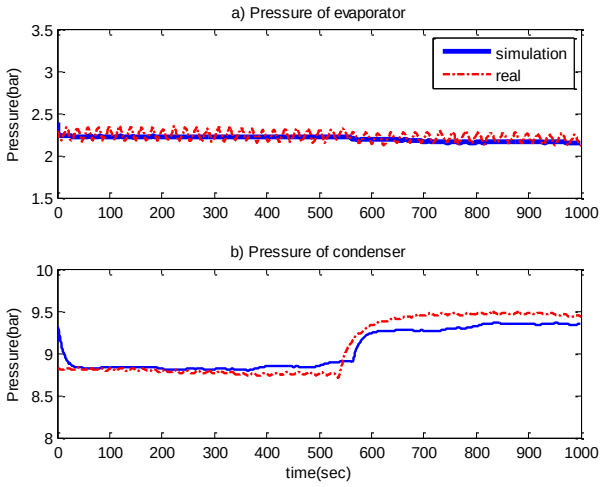

Fig. 20. Pressures of evaporator and condenser

Table 2 The MPAE between simulation and test data

Parameters	*MAPE* (%)
Evaporator pressure	2.77
Condenser pressure	1.06
Refrigerant temp at outlet of Condenser	1.66
Refrigerant temp at inlet of Condenser	0.96
Refrigerant temp at outlet of evaporator	8.66
Refrigerant temp at inlet of evaporator	8.43
Air temp at outlet of evaporator	8.69
Air temp at outlet of condenser	3.27

The comparison results are given in the form of the mean absolute percentage error (MPAE) in Table 2. The value is the average of the three scenarios. From the results, it can be seen that the model prediction is accurate and can be used in MPC development.

7. Controller Development

In order to further show that the proposed model has enough accuracy to be utilized for controller development and can serve as a basis to evaluate other controllers, the on/off controller is developed firstly and its simulation and experimental results are compared. Due to its simplicity and ease to apply, the on/off controller is popular and extensively used currently. However, its nature also leads to the following drawbacks: first, it is unable to regulate the temperature oscillation amplitudes upon changing conditions, such as ambient temperature and varying food temperature requirements, so it may amplify food deterioration or make people feel uneasy. Second, frequent compressor on/off activations can lead to excessive power consumption and cause mechanical components to wear over time [5]. More importantly, energy saving is not considered in the on/off controller, which is the reason to develop more advanced controllers for automotive A/C-R system.

7.1. On/off Controller

For the controller application, the model of the evaporator-side chamber should be integrated into the A/C-R system models. From Fig. 5, it can be seen that the chamber used is a 2 m^3 wooden chamber to represent the cargo for a truck. The inside air temperature of the cargo is one of the control objectives whose dynamics can be shown approximately by the following equation,

$$\frac{dT_{cargo}}{dt} = \frac{\dot{Q}_{inconv} + \dot{Q}_{inf} + \dot{Q}_{door} - \dot{Q}_{vcc}}{(MC)_{air}} \tag{15}$$

where, $\dot{Q}_{inconv}$ represents the convective heat transfer from the interior surface; $\dot{Q}_{door}$ and $\dot{Q}_{inf}$ are the extra load due to opening the door during delivery and infiltration load respectively, and $\dot{Q}_{vcc}$ is the cooling capacity produced by the A/C-R system to balance the heating load from outside [15]. In the simulation and experimental work, the first two parameters will be treated together and

identified by test data as the heating load from outside. $\dot{Q}_{door}$ as the extra heating load or the disturbance will be added by to experiment process by a heater. $(MC)_{air}$ is the thermal inertial of the air inside the whole cargo space.

The following logic rules can be employed to demonstrate the basic idea:

1) If the current evaporator-side chamber temperature is higher than the upper band, the compressor will be turned on.
2) If the current evaporator-side chamber temperature is lower than the lower band, the compressor will be shut down.
3) If the current evaporator-side chamber temperature is between the upper and lower band, the compressor state will remain unchanged.

The operating conditions and initial values of some parameters under two scenarios are listed in Table 3.

Table 3 Operating and initial conditions

Parameters	*Scenario 1*	*Scenario 2*
Ambient temperature $(°C)$	25	25
Evaporator-side chamber initial temp $(°C)$	23	23
Temperature set point $(°C)$	16	17
Heating load (kw)	0.65	0.65
Door opening extra heating (kw)	0.15	0.15
Evaporator fan speed (Hz)	40	40
Condenser fan speed (Hz)	40	40
Compressor pump speed (rpm)	4500	4500

From Fig. 21 and Fig. 22, it can be seen that the simulation results are in agreement with the experimental test. This can also show the accuracy of the model. In addition, this model can run about 30 times faster than in real time on a regular computer compared to the 1.56 times proposed in [18].

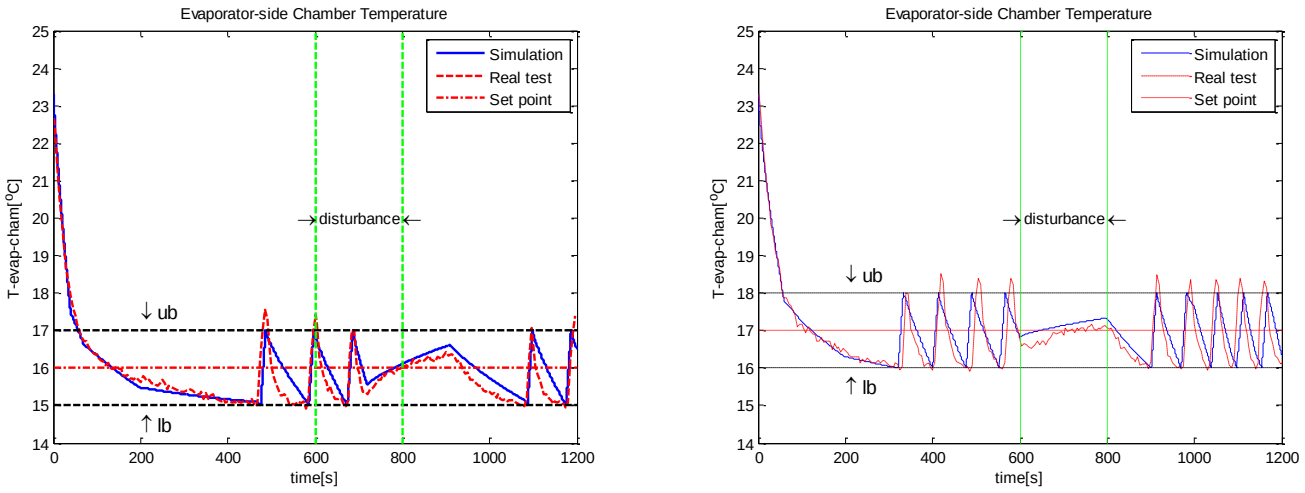

Fig. 21. Evaporator-side chamber temperature performance

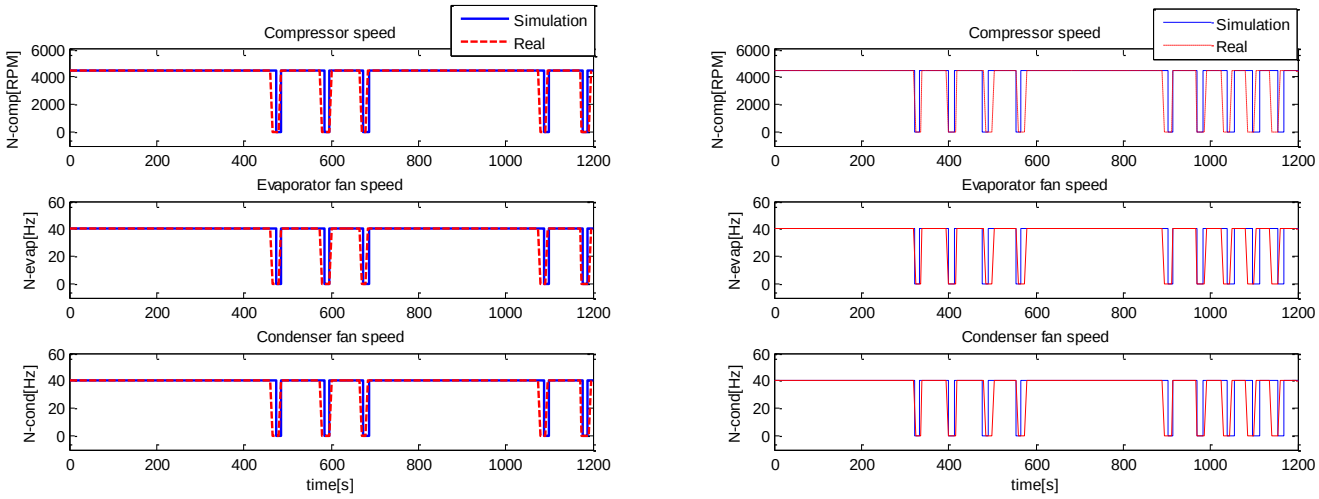

Fig. 22. System inputs

7.2. Discrete MPC Development

As is known, the A/C-R system is a highly nonlinear MIMO with slow dynamics. If the nonlinear system model is directly used for an MPC controller design, its computational efficiency is extremely low such that the nonlinear MPC cannot be implemented on a real-time microcontroller. To solve this problem, a linear MPC will be developed in this paper. The whole procedure, including model linearization, discretization as well as objective function reformulation is elaborated in [29]. The main idea is that an optimization problem should be solved at each time instant. By introducing a prediction of horizon length and control horizon length N, the discretized objective function in next N steps will be formulated,

$$J(x_0,u_0) = e(N)^T Pe(N) + \sum_{k=0}^{N-1} e(k)^T Qe(k) + \Delta u(k)^T S\Delta u(k)$$

$$\text{with, } e(k) = y(k) - y_{ref}(k), \quad k = 1,2,\dots N$$

$$s.t. \tag{18}$$

$$x_{min} \le x(k) \le x_{max}$$
$$u_{min} \le u(k) \le u_{max}$$
$$\Delta u_{min} \le \Delta u(k) \le \Delta u_{max}$$

where the first item, *i.e.*, the final state costs, and the last item, *i.e.*, the increment of inputs, are added to the above function in order to make the controller more stable. Meanwhile the optimization problem is always subjected to some constraints. Finally, the objective function (Equation (18)) of this tracking problem is transferred into quadratic form with respect to the increment of control inputs in order to prepare to use the convex quadratic programming problem solver [30]. The convex quadratic objective function only with respect to the increment of input item is obtained by using the linearized and discretized system model and reformulating the original objective function shown in Equation (18) by:

$$J(x_0,u_0) = \frac{1}{2}\Delta\bar{U}^T H\Delta\bar{U} + \Delta\bar{U}^T g \tag{19}$$

$$s.t.$$

$$\Delta\bar{U} \ge max\left(\Delta\bar{U}_{min}(U), \Delta\bar{U}_{min}(\Delta\bar{U})\ \Delta\bar{U}_{min}(X)\right),\ \Delta\bar{U} \le min\left(\Delta\bar{U}_{max}(U), \Delta\bar{U}_{max}(\Delta\bar{U})\ \Delta\bar{U}_{max}(X)\right)$$

where the Hessian matrix (H) is symmetric and positive or semi-positive definite and the g is the gradient vector. The constraints shown in Equation (18) are also reformulated into the ones only related to the increment of system inputs. After solving the above problem, the first element of the optimal solution will be applied to the real system. This linear *MPC* is built into Matlab/SIMULINK and its structure is shown in Fig. 23, where the lookup tables are used to implement thermodynamic properties of the refrigerant. Then, several unknown parameters are identified and sent to the algorithm and the solver together with all other known information.

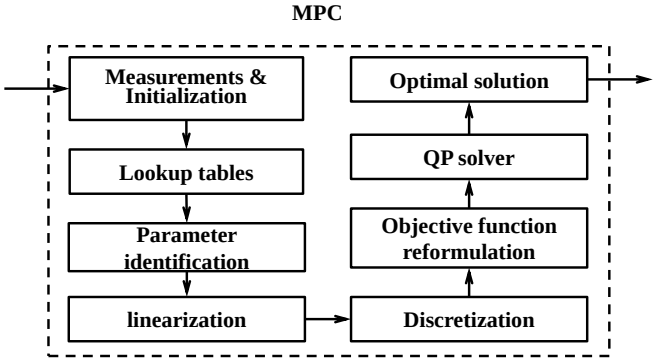

Fig. 23. Structure of MPC

In this linear MPC, the constraints of system inputs and controller parameters are shown in Table 4, where the time step length (T_s) is used for simulation while the actual time used for one step simulation is only 0.04s on a regular computer, which is fast enough for real-time implementation.

Table 4 Inputs constraints and Linear MPC parameter values

$N_{comp}(rpm)$	$N_{evap}(Hz)$	$N_{cond}(Hz)$	$T_s(s)$	Q	N	P	R	S
$\begin{bmatrix}2500\\3500\\4500\end{bmatrix}$	$[0 \sim 40]$	$[0 \sim 40]$	5	100000	10	$1000Q$	$\begin{bmatrix}5? & 0\\0\ 0 & 0\\0\ 0 & 0\end{bmatrix}$	$\begin{bmatrix}0 & 0 & 0\\0 & 1000 & 0\\0 & 0 & 1000\end{bmatrix}$

Because of the existence of the discrete input compressor speed, a discrete MPC is developed, which is composed of three sub-MPCs as shown in Fig. 24. Three sub-MPCs are running simultaneously at three different compressor speeds (2500, 3500 and 4500 rpm) to find the optimal solutions of other two inputs. Then, three best cost values are recalculated by the two optimal input values as well as the corresponding compressor speed. By comparing their values, the minimum one will be the optimal cost of the current time instant and the corresponding input values are the optimal solution. For example, if the J_{3500} is the minimum cost value, then the optimal solution is the combination of 3500 rpm (N_{comp}) as well as the optimal values of N_{evap} and N_{cond} founded by MPC_3500 .

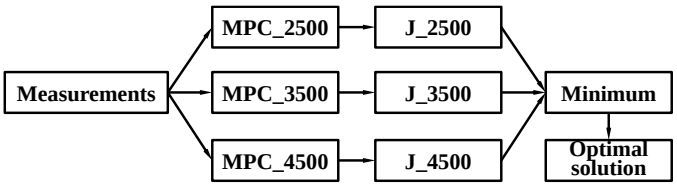

Fig. 24. Structure of the discrete MPC

The simulation results are presented in Fig. 25 and Fig. 26. It can be seen from the results that the chamber temperature quickly settles down and stay there. Under the period of large disturbance brought by extra heating load, the controller tries to maintain the temperature at its set point by increasing evaporator fan speed as well as the condenser one instead of changing the compressor speed, which is largely related to the energy consumption. That is why a large weight was chosen for compressor speed increment. This weight should be decreased or Q be increased if one puts more emphasis on temperature performance. The simulation time for the MPC is much shorter than real time, which means this controller could be applied into the real control system.

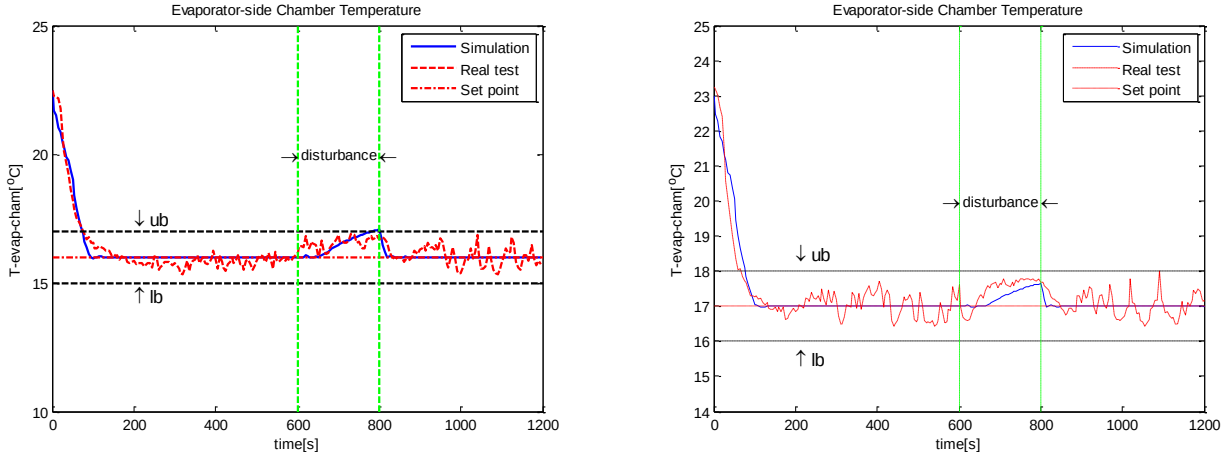

Fig. 25. Controlled temperature performance

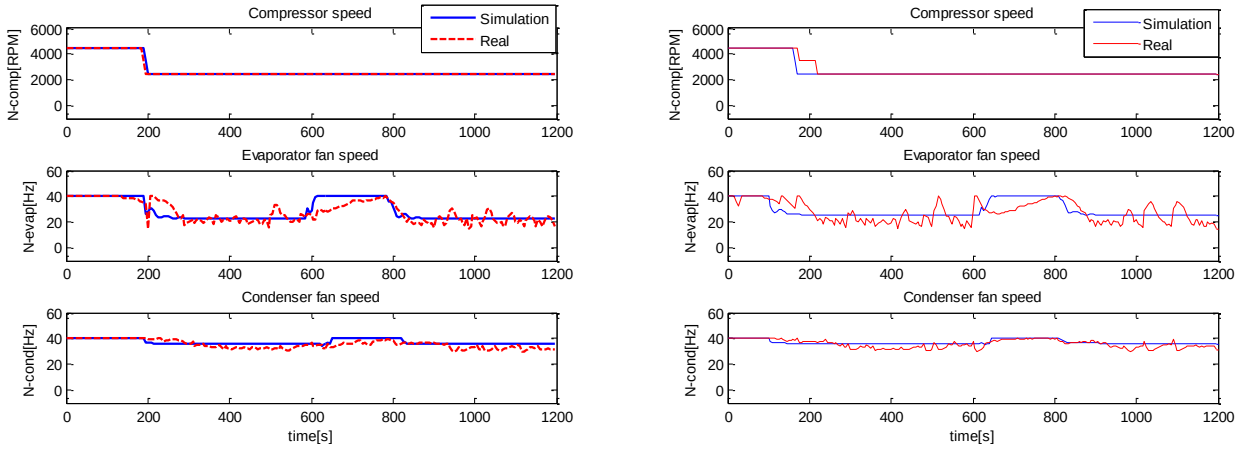

Fig. 26. Three inputs of the system

7.3. Comparison

In order to demonstrate the advantage of the MPC, the results of on/off control and MPC are compared from several aspects by using MAPE.

Table 5 Results comparison of controllers

Controllers performance	*Scenario 1*		*Scenario 2*	
	On/off	*MPC*	*On/off*	*MPC*
MAPE between real and simulation	1.6%	3.14%	1.92%	1.72%
MAPE between simulation and set point	4.36%	3.37%	4.20%	3.00%
Max APE	9.63%	5.76%	8.9%	5.91%
Controller performance	Bad	Good	Bad	Good
Energy consumption (Kwh-1200s)	0.2063	0.1902	0.2041	0.1793
Energy Improvement	0	7.8%	0	10.33%

Obviously, the temperature performance of the *MPC* is better than that of the conventional on/off controller not only during the dynamic period but also in the steady state region from the above figures. By data analysis, the values in Table 5 can draw a more convinced conclusion that both the set-point controller and MPC bring better performance than the conventional two. More specifically, the first MAPE measures the deviation between real and simulation temperature responses. The small MAPE values mean that the model used for the controller development has a high accuracy. The second MAPE demonstrates the offset between the temperature response and its set point, whereas the maximum APE shows the largest drift of the temperature from its set point. It can be seen that the on/off controller has worse performance than MPC.

8. CONCLUSIONS

The goal of this study was to design an advanced energy efficient controller for an automotive A/C-R system to bring benefits for both vehicle owners and environment.

Firstly, a control-based model was developed that not only reflects the dominant dynamics of an A/C-R system but was also simple enough to be used in real-time controllers. The model is a trade-off between accuracy of a full detailed thermodynamics model and simplicity needed for a real time controller. The proper modeling of heat exchangers is vitally important in capturing the overall dynamics of A/C-R systems. The effects of fins in the heat transfer process of heat exchangers were considered to improve the accuracy of A/C-R models. The fins' effects were lumped into the equivalent parameters to keep the simplicity of the model. The parameters, however, could be identified directly from experimental data. Unlike the existing model, the effects from the superheat section of condenser were also integrated into the proposed model to guarantee its accuracy. Then, the experimental analysis shows that the model can correctly predict the complex behavior of an A/C-R system. Thanks to its simplicity, it can be easily used in real-time controllers.

Finally, to further demonstrate its accuracy and achieve its optimal performance, the popularly used on/off controller was designed, which also serves as a basis to compare with other controllers. Simulation and experimental results showed that the proposed discrete MPC is capable of improving the performance of controlled temperature while saving about 8% energy compared to the conventional controller under the examined scenario. The proposed MPC can bring more fuel saving to the owners as well as the

environment.

9. Acknowledgements

The authors would like to acknowledge the financial support of Automotive Partnership Canada (APC) along with the financial and technical support of Cool-it Group.

10. Appendix I

The complete nonlinear and linearized models at the current operating point are given in the following table.

$\dot{x}$	$f(x,u)$	f_{12x}	$\left(\dot{m}_v \frac{dh_{ge}}{dP_e} + \alpha_i A_i \frac{l_e}{L_e}\frac{dT_{re}}{dP_e}\right) \Big/ \left(\rho_{le} h_{lge} A_e (1-\bar{\gamma}_e)\right)$
y	$g(x,u)$	f_{13x}	$-\alpha_i A_i l_e \Big/ \left(\rho_{le} h_{lge} A_e (1-\bar{\gamma}_e) L_e\right)$
u	$\left[N_{comp}, N_{evap}, N_{cond}\right]^T$	f_{22x}	$\left(\dot{m}_v \frac{dh_{le}}{dP_e} - \alpha_i A_i \frac{l_e}{L_e}\frac{dT_{re}}{dP_e}\right) \Big/ \left(h_{lge} A_e L_e \frac{d\rho_{ge}}{dP_e}\right)$
x	$\left[l_e, P_e, T_{we}, P_c, T_{wc}, T_{cargo}\right]^T$	f_{23x}	$\alpha_i A_i l_e \Big/ \left(h_{lge} A_e L_e^{\,2} \frac{d\rho_{ge}}{dP_e}\right)$
y	T_{cargo}	f_{24x}	$\dot{m}_v \frac{dh_{le}}{dP_c} \Big/ \left(h_{lge} A_e L_e \frac{d\rho_{ge}}{dP_e}\right)$
$f = \begin{bmatrix} f_1 \\ f_2 \\ f_3 \\ f_4 \\ f_5 \\ f_6 \end{bmatrix}$	$\begin{bmatrix} \left(\dot{m}_v (h_{ge} - h_{le}) - \alpha_{ie}\pi D_{ie} l_e (T_{wfe} - T_{re})\right) \Big/ \left(\rho_{le} h_{lge} A_e (1-\bar{\gamma}_e)\right) \\ \left(\dot{m}_v \frac{h_{ie} - h_{le}}{h_{lge}} - \dot{m}_{comp} + \frac{\alpha_{ie}\pi D_{ie} l_e (T_{wfe} - T_{re})}{h_{lge}}\right) \Big/ \left(A_e L_e \frac{d\rho_{ge}}{dP_e}\right) \\ \left(\alpha_{oe} A_{be} (T_{ae} - T_{wfe}) - \alpha_{ie}\pi D_{ie} l_e (T_{wfe} - T_{re}) - \alpha_{iesh}\pi D_{ie} (L_e - l_e)(T_{wfe} - T_{re})\right) \Big/ (C_p m)_{we} \\ \left(\dot{m}_{com} - \frac{\alpha_{ic}\pi D_{ic} l_c (T_{rc} - T_{wc})}{h_{lgc}}\right) \Big/ \left(A_c L_c \frac{d\rho_{gc}}{dP_c}\right) \\ \left(\dot{m}_{comp} - \frac{\alpha_{ic}\pi D_{ic} l_c (T_{rc} - T_{wfc})}{h_{lgc}}\right) \Big/ (C_p m)_{wc} \\ \left(\dot{Q}_{out} - \alpha_o A_o l_e (T_a - T_{we})\right) \Big/ (MC)_{air} \end{bmatrix}$	f_{32x}	$\alpha_i A_i \frac{dT_{re}}{dP_e} \Big/ (C_p m)_{we}$
		f_{33x}	$-\alpha_i A_i + \alpha_o A_o \left(\frac{dT_a}{dT_{we}} - 1\right) \Big/ (C_p m)_{we}$
		f_{36x}	$\alpha_o A_o \left(\frac{dT_a}{dT_{cargo}}\right) \Big/ (C_p m)_{we}$
		f_{41x}	$-\alpha_{ic} A_{ic} (T_{rc} - T_{wc}) \frac{\partial l_c}{\partial l_e} \Big/ \left(h_{lgc} A_c L_c^{\,2} \frac{d\rho_{gc}}{dP_c}\right)$
		f_{44x}	$-\alpha_{ic} A_{ic} l_c \frac{dT_{rc}}{dP_c} \Big/ \left(h_{lge} A_c L_c^{\,2} \frac{d\rho_{gc}}{dP_c}\right)$
		f_{45x}	$\alpha_{ic} A_{ic} l_c \Big/ \left(h_{lge} A_c L_c^{\,2} \frac{d\rho_{gc}}{dP_c}\right)$
$g(x,u)$	x_6	f_{54x}	$\alpha_{ic} A_{ic} \frac{dT_{rc}}{dP_c} \Big/ (C_p m)_{wc}$
A_c	$\begin{bmatrix} f_{11x} & f_{12x} & f_{13x} & f_{14x} & 0 & 0 \\ f_{21x} & f_{22x} & f_{23x} & f_{24x} & 0 & 0 \\ 0 & f_{32x} & f_{33x} & 0 & f_{35x} & 0 \\ f_{41x} & 0 & 0 & f_{44x} & f_{45x} & 0 \\ 0 & 0 & 0 & f_{54x} & f_{55x} & 0 \\ f_{61x} & 0 & f_{63x} & 0 & 0 & f_{66x} \end{bmatrix}$	f_{55x}	$-\alpha_{ic} A_{ic} + \alpha_{oc} A_{oc} \left(\left(\frac{dT_{ac}}{dT_{wc}} - 1\right)\right) \Big/ (C_p m)_{wc}$
		f_{61x}	$-\alpha_o A_o (T_a - T_{we}) / (MC)_{air}$
		f_{63x}	$-\alpha_o A_o l_e \left(\frac{dT_a}{dT_{we}} - 1\right) \Big/ (MC)_{air}$
		f_{66x}	$-\alpha_o A_o l_e \left(\frac{dT_a}{dT_{cargo}}\right) \Big/ (MC)_{air}$
B_c	$\begin{bmatrix} f_{11u} & 0 & 0 \\ f_{21u} & f_{22u} & 0 \\ 0 & 0 & f_{33u} \\ 0 & f_{42u} & 0 \\ 0 & 0 & 0 \\ 0 & 0 & f_{63u} \end{bmatrix}$	f_{11u}	$-(h_{ie} - h_{ge}) \frac{d\dot{m}_v}{du_v} \Big/ \left(\rho_{le} h_{lge} A_e (1-\bar{\gamma}_e)\right)$
		f_{21u}	$\frac{h_{ie} - h_{le}}{h_{lge}} \frac{d\dot{m}_v}{du_v} \Big/ \left(A_e L_e \frac{d\rho_{ge}}{dP_e}\right)$
		f_{22u}	$-\frac{d\dot{m}_{comp}}{dN_{comp}} \Big/ \left(A_e L_e \frac{d\rho_{ge}}{dP_e}\right)$
		f_{33u}	$\left(\frac{d\alpha_o}{dN_{evap}} A_o (T_a - T_{we}) + \alpha_o A_o \frac{dT_a}{d\alpha_o}\frac{d\alpha_o}{dN_{evap}}\right) \Big/ (C_p m)_{we}$
C_c	$\begin{bmatrix} 0 & 0 & 0 & 0 & 0 & 1 \end{bmatrix}$	f_{42u}	$\frac{d\dot{m}_{comp}}{dN_{comp}} \Big/ \left(A_c L_c \frac{d\rho_{gc}}{dP_c}\right)$

f_{11x}	$-\alpha_i A_i (T_{we} - T_{re}) / \rho_{le} h_{lge} A_e (1-\bar{\gamma}_e) L_e$	f_{63u}	$\left(-\frac{d\alpha_o}{dN_{evap}} A_o l_e (T_a - T_{we}) - \alpha_o A_o l_e \frac{dT_a}{d\alpha_o} \frac{d\alpha_o}{dN_{evap}} \right) \Big/ \left((MC)_{air} \right)$

11. References

[1] Dinçmena E and Güvenç BA. A control strategy for parallel electric vehicles based on extreme seeking. *Vehicle System Dynamics: International Journal of Vehicle Mechanics and Mobility*. Feb. 2012; vol. 50, No. 2, p. 199-227.

[2] Lust EE. System-level analysis and comparison of long-haul truck idle-reduction technologies. MASc Thesis, University of Maryland, USA, 2008.

[3] Morshed MR. Unnecessary Idling of Vehicles: An analysis of the current situation and what can be done to reduce it. MASc Thesis, McMaster University, CANADA, 2010.

[4] Khayyama H, Nahavandia S, Hub E et al. Intelligent energy management control of vehicle air conditioning via look-ahead system. *Applied Thermal Engineering* 2011; 16: pp.3147-3160.

[5] Liu JY, Zhou HL and Zhou XG. Automotive air conditioning control- A survey. *International Conference on Electronic & Mechanical Engineering and Information Technology* 2011; 7: pp. 3408-3412.

[6] Fabio Chiara and Marcello Canova. A review of energy consumption, management, and recovery in automotive systems, with considerations of future trends. *Proc. IMechE Vol. 227 Part D: J Automobile Engineering*, 2013, 6: pp. 914-936.

[7] Heide Budde-Meiwes, Julia Drillkens, Benedikt Lunz, Jens Muennix. A review of current automotive battery technology and future prospects. *Proc. IMechE Vol. 227 Part D: J Automobile Engineering*, 2013, 5: pp. 761-776.

[8] Rajit Johri and Zoran Filipi. Optimal energy management of a series hybrid vehicle with combined fuel economy and low-emission objectives. *Proc. IMechE Vol. 228 Part D: J Automobile Engineering*, 2014, 12: pp. 1424-1439.

[9] Jalaliyazdi, M., Khajepour, A., Chen, S., and Litkouhi, B. Handling Delays in Stability Control of Electric Vehicles Using MPC. *SAE Technical Paper* 2015; doi: 10.4271/2015-01-1598.

[10] Kania, M., Koeln, J., Alleyne, A., McCarthy, K. et al. A Dynamic Modeling Toolbox for Air Vehicle Vapor Cycle Systems. *SAE Technical Paper* 2012; doi: 10.4271/2012-01-2172.

[11] He XD. Dynamic Modeling and Multivariable control of Vapor Compression Cycles in Air Conditioning Systems. PhD thesis, Massachusetts Institute of Technology, USA, 1996.

[12] MacArthur, JW and Grald, EW. Unsteady Compressible Two-Phase Flow Model for Predicting Cyclic Heat Pump Performance and a Comparison With Experimental Data. *International Journal of Refrigeration* Jan. 1989; Vol. 12, no. 1, pp. 29-41.

[13] Rasmussen BP and Alleyne AG. Dynamic Modeling and Advanced Control of Air Conditioning and Refrigeration Systems. ACRC Technical Report-244, Air Conditioning and Refrigeration Center, University of Illinois, USA, 2006.

[14] Wedekind, GL, Bhatt BL and Beck BT. A system mean void fraction model for predicting various transient phenomena associated with two-phase evaporating and condensing flows. *Int. J. Multiphase Flow* , 1978; Vol.4, pp.97-114

[15] Li B. Dynamic modeling and control of vapor compression cycle systems with shut-down and startup operations. M.S. Thesis, University of Illinois at Urbana-Champaign, USA, 2009.

[16] Eldredge BD and Alleyne AG. Improving the Accuracy and Scope of Control-Oriented Vapor Compression Cycle System Models. ACRC Technical Report-246, Air Conditioning and Refrigeration Center, University of Illinois, USA, 2006.

[17] Fasl JM. Modeling and control of hybrid vapor compression cycles. M.S. Thesis, University of Illinois at Urbana-Champaign, USA, Aug. 2013.

[18] Shah R, Alleyne AG, et al. Dynamic Modeling and Control of Single and Multi-Evaporator Subcritical Vapor Compression Systems. ACRC Technical Report-216, Air Conditioning and Refrigeration Center, University of Illinois, USA, 2003.

[19] Rasmussen BP. Control-oriented modeling of transcritical vapor compression systems. M.S. Thesis, University of Illinois at Urbana-Champaign, USA, 2002.

[20] Li B, Jain N, Mohs WF, Munns S, et al. Dynamic modeling of refrigerated transport systems with cooling-mode/heating-mode switch operations. *HVAC&R Research*, 2012; 18:5: 974-996

[21] McKinley TL, Alleyne AG. An advanced nonlinear switched heat exchanger model for vapor compression cycles using the moving-boundary method. *International journal of refrigeration*, 2008; 31: 1253–1264.

[22] He XD, Liu S, Asada HH, et al. Multivariable control of vapor compression systems. *HVAC&R Research*, 2011; 4:3:205-230.

[23] Lee J, Kim J, Park J, et al. Effect of the air-conditioning system on the fuel economy in a gasoline engine vehicle. *Proc. Vol. 227 IMechE Part D: J Automobile Engineering*, 2013; pp. 66–77.

[24] Aditya Dhand and Keith Pullen. Optimal energy management for a flywheel-assisted battery electric vehicle. *Proc. Vol. 229 IMechE Part D: J Automobile Engineering*, 2015; 12: pp. 1672-1682.

[25] Refrigerant reference guide. WORLWIDE REFRIGERANT SUPPLIER FOURTH EDITION 2004. www.refrigerants.com/catalog.pdf

[26] M M Salim. Potential for expanders in a mobile carbon dioxide air-conditioning system. *Proc. IMechE Vol. 224 Part D: J Automobile Engineering*, 2009, pp. 219–228.

[27] Nejad EK, Hajabdollahi M, Hajabdollahi H. Modeling and Second Law Based Optimization of Plate Fin and Tube Heat Exchanger Using MOPSO. *J Appl Mech Eng*, 2012; 2: 118

[28] Jabardo JM and Mamani WG. Modeling and experimental evaluation of parallel flow micro channel condensers. Journal of the Brazilian Society of Mechanical Sciences and Engineering, 2003; vol.25 no.2.

[29] Borrelli F, Bemporad A and Morari M, "Predictive Control for linear and hybrid systems," 2014.

[30] Ferreau HJ, et al, "qpOASES User's Manual," Version 3.0 beta. March 2014.